Transforming Boron Carbon Nitride: A Carbon-to-Oxygen Switch to Boost Propane Oxidative Dehydrogenation

Xinping Zhang,[†] Bohua Ren,[†,‖,*] Zhenzhen Yang,[⊥] Hao Chen,[†,*] and Sheng Dai[⊥,*]

[†]State Key Laboratory for Chemo/Biosensing and Chemometrics, College of Chemistry and Chemical Engineering, Hunan University, Changsha, 410082, China

[‖]State Key Laboratory of Powder Metallurgy, College of Chemistry and Chemical Engineering, Central South University; Changsha 410083, China

[⊥]Chemical Sciences Division, Oak Ridge National Laboratory, Oak Ridge, TN 37831, USA

Supporting Information Placeholder

ABSTRACT: Hexagonal boron nitride (h-BN) catalysts exhibit promising olefin selectivity in the oxidative dehydrogenation of propane (ODHP). However, their catalytic activity is limited by the intrinsically low density of active B–O sites in the h-BN scaffolds. An in situ carbon-to-oxygen switch strategy with a well-defined boron carbon nitride (BCN) skeleton was developed to afford h-BN catalysts with abundant BO_3 units, leading to enhanced catalytic performance in ODHP. An ionothermal procedure was adopted for BCN construction from molten salt precursors ($NaNH_2$, $NaBH_4$, and CaC_2), in which the uniformly embedded $B–C_3$ was transformed into $B–O_3$ via oxidative calcination (denoted as BON). The structural evolution from BCN to BON was well characterized by spectroscopy and soft X-ray-based techniques. The abundant number of BO_3 units in the as-afforded BON catalysts led to significantly enhanced catalytic performance in ODHP, outperforming the commercial and molten salt-derived h-BN catalysts, with 50.4% conversion of propane and 32.7% yield of olefins achieved at 500 °C. Theoretical simulations further revealed that these $B–O_3$ species ensure the preferential adsorption and dissociation of the C–H bonds of propane, making the process more thermodynamically favorable. The ionothermal and in situ restructuring approach developed herein provides an efficient strategy to afford high-quality heteroatom-doped h-BN catalysts with enhanced performance in diverse catalysis procedures.

Propylene is a crucial chemical building block in the petrochemical industry and is traditionally produced through fluid catalytic cracking, steam cracking of hydrocarbons in naphtha, and the methanol-to-olefin process.[1-3] Propane dehydrogenation (PDH) has emerged as a promising industrial method for propylene production, particularly following the "shale revolution," which offers the additional benefit of sustainable hydrogen recycling.[4-7] Nevertheless, PDH faces challenges, including the formation of undesired byproducts from cracking and coke formation. These issues arise from the endothermicity of the reaction, which requires high temperatures.[8] In contrast, the oxidative dehydrogenation of propane (ODHP) offers a competitive alternative for propylene production. The ODHP is favored for its exothermicity and ability to suppress coking. Extensive research has focused on metal oxide-based catalysts for ODHP. However, olefins tend to overoxidize, resulting in byproducts such as monoxide (CO) and carbon dioxide (CO_2). This overoxidation is a critical limitation for the industrial implementation of the ODHP.[9-11]

Hexagonal boron nitride (h-BN), one of the most promising materials composed of alternating B and N atoms via strong B–N bonds, has emerged as a vital two-dimensional (2D) nanomaterial analogous to graphene with planar structures.[12,13] The unique linking pattern endows h-BN with adjustable chemical, electrical, and optical properties, enabling high performance in various fields.[14-16] In 2016, h-BN and boron nitride nanotubes (BNNTs) were identified as promising catalysts for ODHP, exhibiting unprecedented olefin selectivity.[17,18] Research has demonstrated that the formation of boron-oxygen active phases, such as BO_3 and >BO–OB< species, during ODHP pretreatment is crucial for catalytic activity.[19-22] However, the intrinsic limitation in the number of active sites typically formed at unsaturated B sites at the edges and defects in h-BN results in low catalytic activity.[23] To address this issue, a progressive substitution strategy was introduced under high-temperature conditions (>1,500 °C) to develop boron-oxygen-nitrogen nanotubes (BONNTs) enriched with in situ formation of $B–O_3$ and O–O species as highly active, selective, and stable catalysts for ODHP.[24] Further studies on supported boron oxide catalysts (B_2O_3/SiO_2) have presented promising results for ODHP featuring BO_3 and BO–H species.[25] Additionally, an economically viable oxidized activated carbon-supported boron (B/OAC) with stable 3-coordinate BO_3-containing species showed high activity in ODHP,[26] followed by rapid loss of bulky B_2O_3. Consequently, the construction of stable B–O active sites plays a crucial role in enhancing ODHP performance. Therefore, developing a

simple and controllable method for preparing h-BN nanomaterials enriched with B–O active sites for ODHP remains both essential and challenging.

In this study, we present an in situ carbon-to-oxygen switch strategy in a well-defined boron carbon nitride (BCN) skeleton, in which the uniformly embedded $B–C_3$ was transformed into $B–O_3$ via oxidative calcination (denoted as BON). The incorporation of C was achieved through a thermal method involving inorganic molten salts, utilizing $NaNH_2$, $NaBH_4$ and CaC_2 as precursors to produce h-BCNs, in which the C atoms act as $B–C_3$ in h-BN[27]. Subsequently, the C atoms in BCN were substituted with O atoms via pyrolysis in O_2 atmospheres, successfully yielding abundant $B–O_3$ sites in the h-BN skeleton, offering a significant improvement in ODHP activity. The as-afforded boron-oxygen-nitride (h-BON-1) offers an olefin yield of 32.7% and a propane conversion of 50.4% under a WHSV of 7200 h^{-1} at 500 °C, which is 2.4 times greater than that of commercial h-BN. In situ diffuse reflectance infrared Fourier transform spectroscopy (DRIFTs) and density functional theory (DFT) calculations revealed that the in situ formation of $B–O_3$ active species facilitates the preferential adsorption and activation of C–H bonds and is thermodynamically favorable for the formation of C=C bonds during ODHP. The controlled incorporation of C atoms into the h-BN framework provides a promising avenue for designing highly efficient catalysts for ODHP and constructing BCN nanostructures with tunable compositions and good crystallinity.

The h-BCN materials were constructed using $NaBH_4$, $NaNH_2$, and CaC_2 as starting materials, followed by pyrolysis under O_2 atmospheres to substitute C atoms with O atoms in situ to synthesize h-BON, which resulted in the formation of abundant $B–O_3$ active species in h-BON (see Figure 1A and the experimental procedures in the Supporting Information). The presence of C domains typically led to darker composites, so the color of the product deepened with increasing amounts of CaC_2[28] (Figure S1). Thermogravimetric analysis (TGA) revealed that the C contents in h-BCN-1, h-BCN-2, and h-BCN-3 were 3.7 wt%, 6.5 wt%, and 12.0 wt%, respectively (Figure S1). X-ray diffraction (PXRD) results of the synthesized h-BCN materials revealed a prominent diffraction peak at 2θ = 26.31°, corresponding to the (002) crystal plane of h-BN.

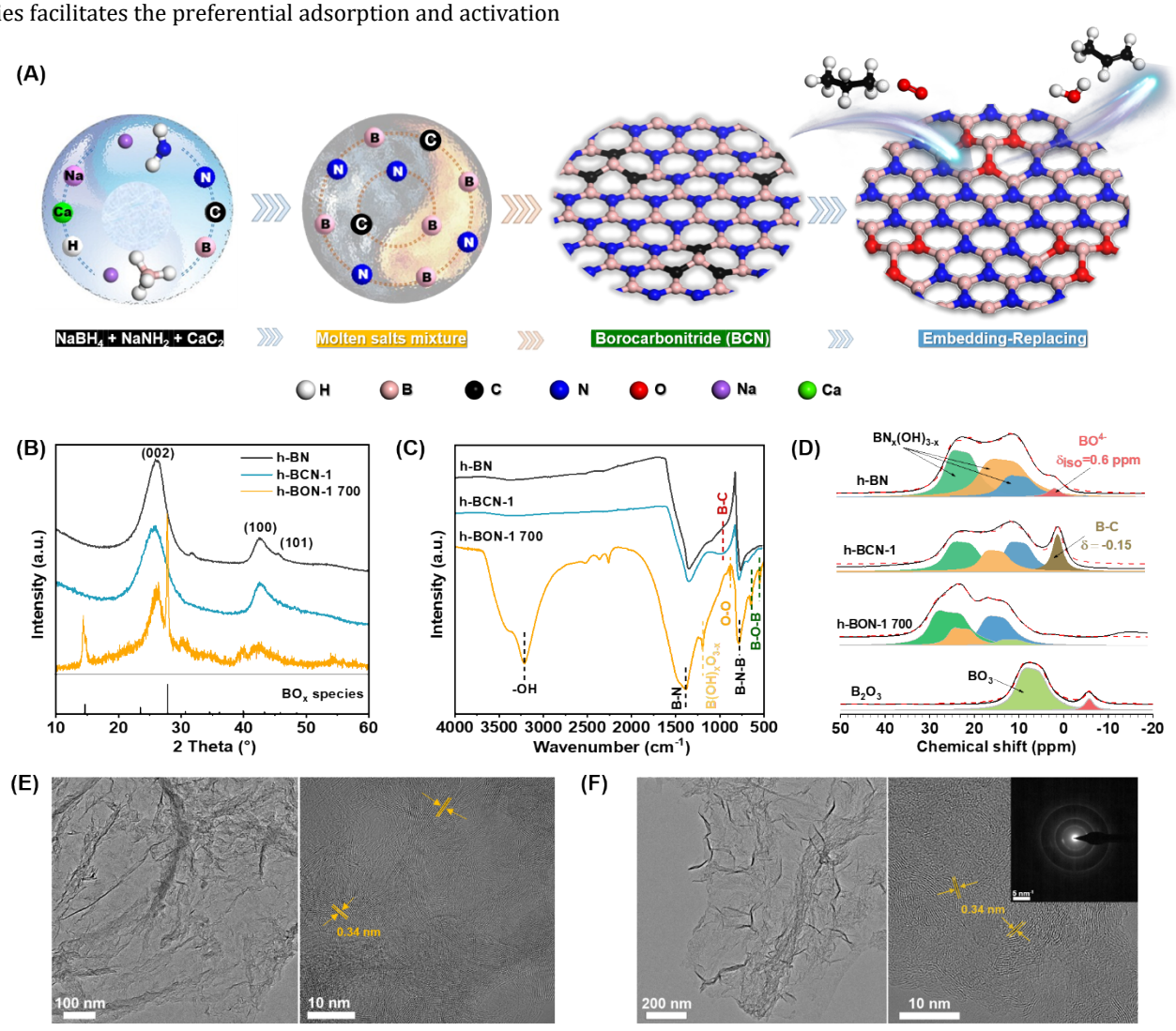

Figure 1. (A) Schematic illustration of the synthesis of h-BCNs and h-BON through a carbon embedding-oxygen replacing strategy to transfer $B–C_3$ to $B–O_3$ in boron nitride. (B) XRD patterns and (C) FTIR spectra of h-BN, h-BCN-1 and h-BON-1. (D) ^{11}B solid-state NMR spectra of h-BN, h-BCN-1, h-BON-1, and B_2O_3. HR-TEM images of (E) h-BCN-1 and (F) h-BON-1.

Additionally, two weaker peaks attributed to the (100) and (101) crystal planes at 2θ = 42.4° and 45.5°, respectively, diminished with increasing embedded C content, ultimately indicating a decrease in crystallinity (Figure 1B, Figure S2). These results confirmed that the introduction of C atoms into the h-BN lattice induced an amorphization effect.[29] Furthermore, the h-BON-1 pattern exhibited a broad peak corresponding to lower crystalline h-BN and expansion of the interplanar crystal spacing, which was attributed to the substitution of O atoms in the h-BN lattice.[30] Notably, diffraction peaks at 2θ = 27.8° and 39.9° corresponding to BO_x were observed.

The Fourier transform infrared (FTIR) spectra of both h-BN and h-BCNs showed two characteristic peaks at 1,360.2 cm^{-1} and 783.1 cm^{-1}, corresponding to the in-plane stretching and out-of-plane bending vibrations of B–N bonds, respectively. (Figure 1C, Figure S3). An additional peak at 916.2 cm^{-1}, which intensified with increasing C content, was assigned to the B–C bond.[31,32] Moreover, a small peak at 1,643.4 cm^{-1} in in h-BCN-3 indicated the formation of C=N bonds.[33] These results confirmed the successful incorporation of C atoms into the BN lattice to create h-BCN hybrid materials. The FTIR spectrum of h-BON-1 indicated that the h-BN skeleton remained well preserved, even after O_2 activation of h-BON-1 (Figure S4). Additionally, the B–C bonds in the FTIR spectra disappeared after pyrolysis at temperatures higher than 700 °C, and additional absorption peaks assigned to different kinds of B–O active species for ODHP were observed (Figure S5, Figure 1C).[34] Specifically, two absorption peaks at approximately 548.2 cm^{-1} and 647.3 cm^{-1} corresponding to the B–O–B bond were derived from the in situ construction of O-containing terminal groups.[24] Furthermore, the $B(OH)_xO_{3-x}$ species at ~1,195.9 cm^{-1} and O–O species at 926.3 cm^{-1} were detected, indicating that C primarily existed as $B–C_3$ in the h-BN framework, with neighboring C atoms substituted by O atoms.[18,24] In contrast, the vibrations of O–O species and $B(OH)_xO_{3-x}$ species were difficult to recognize in commercial h-BN and h-BN without any C-to-O switching (Figure S6). Thus, C embedding was a crucial step for constructing $B–O_3$ active species. In addition, the strong and broad peaks centered at 3220 cm^{-1} and 3400 cm^{-1} were related to O–H and N–H stretching vibrations, which are features of hydroxylation under the ODHP process commonly observed in the BN system. The ^{11}B solid-state nuclear magnetic resonance (^{11}B SSNMR) spectra revealed three major characteristic signals attributed to B atoms with three coordinating N/O atoms ($BN_x(OH)_{3-x}$ ($0 \le x \le 3$)) that can be simulated with a chemical shift (δ_{iso}) between 31.5 ppm and 14.0 ppm (Figure 1D).[18,35,36] The new signal at 0.60 ppm was attributed to B with hydroxyl groups and B-containing complexes (BO^{4-}), which is consistent with previous studies on h-BN.[27] Notably, h-BCN-1 exhibited an additional peak at -0.15 ppm belonging to the B–C bonds.[37] In addition, from h-BCN-1 to h-BCN-3, the intensity of the B–C peak increased as the C content gradually increased, as shown in Figure S7, indicating that more B–C bonds formed. The difference in the ^{11}B SSNMR data of h-BON-1 and commercial B_2O_3 suggested that the fine structure of the BO_3 species in h-BON-1 did not match that of bulk B_2O_3. These BO_3 species increase with increasing pyrolysis temperature, following the loss of some boron sites (Figure 1D, Figure S8). Hence, these BO_x species were $B–O_3$ in the h-BN structure, not bulk B_2O_3, as confirmed by the FTIR and ^{11}B SSNMR results (Figure S8-S9).

High-resolution transmission electron microscopy (HR-TEM) images revealed a curled nanosheet-like structure in h-BCN-1 (BN: C = 1: 0.05) with an interlayer crystal lattice spacing of 0.34 nm, which is consistent with h-BN synthesized without CaC_2 (Figure 1E, Figure S10). The morphology of the h-BON-1 nanosheets was clearly preserved even after gradual oxidation, as shown in Figure 1F. However, the presence of excessive C led to the aggregation of the h-BN structure and induced a disordered configuration, which was confirmed by N_2 adsorption–desorption analysis and electron paramagnetic resonance (EPR) spectroscopy (Figure S11-S12).

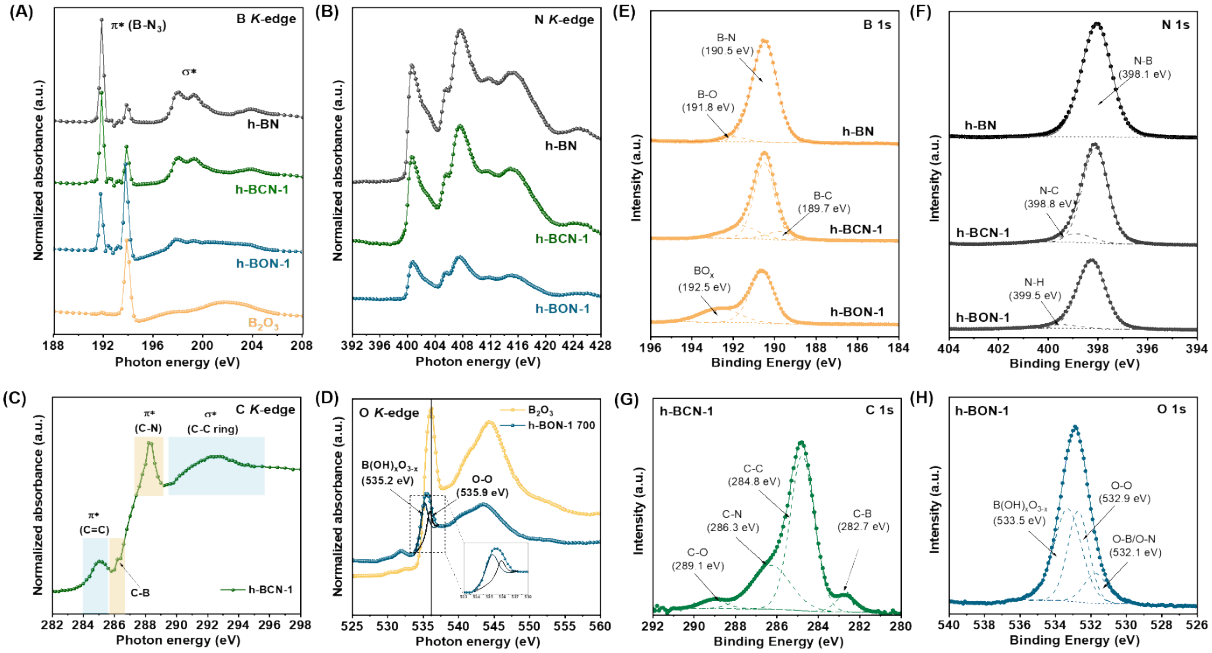

Figure 2. XANES spectra for (A) B K-edges of h-BN, h-BCN-1, h-BON-1, and B_2O_3. (B) N K-edges of h-BN, h-BCN-1, and h-BON-1. (C) C K-edge of h-BCN-1. (D) O K-edge from h-BON-1 and reference B_2O_3. (E) B 1 s XPS spectra and (F) N 1 s XPS spectra of h-BN, h-BCN-1, and h-BON-1. (F) C 1 s XPS spectra of h-BCN-1. (H) O 1 s XPS spectra of h-BON-1.

The transformation of B–C_3 to B–O_3 in the h-BCN framework led to the formation of h-BON-1 nanosheets. X-ray absorption near edge structure (XANES) and X-ray photoelectron spectroscopy (XPS) were employed to gain more insight into the local electronic structures. In the case of the B K-edge, the h-BN, h-BCN-1, and h-BON-1 spectrum curves contained a B 1 s-π* transition resonance at 191.8 eV, indicating the existence of a high concentration of sp^2-hybridization B–N bonds (BN_3), and the broad feature at 197.5 eV corresponded to the B 1 s-σ* transition resonance (Figure 2A). Comparatively, the intensity of the B 1 s π* features in h-BCN-1 decreased compared with that in h-BN (0.25:0.22), indicating that the incorporation of C into the h-BN skeleton significantly reduced the π bonding states by forming defective pyridine-like C–N structures.[38] The peak at 194 eV in fresh h-BON-1 corresponded to a B–O_3 coordination environment, which offered a greater number of reactive sites for ODHP. In contrast, B_2O_3 exhibited a sharp peak at 194 eV (BO_3 species) and broader features above 196 eV, which were considerably different from those of the B–O_3 species in h-BON-1. An intensity decrease trend and assignment was observed in the N K-edge spectrum, which was composed of N 1s-π* transitions (2_{pz}) at 401.7 eV and N 1sσ* transitions ($2p_{x,\ y}$) above 408.6 eV with increased intensity (Figure 2B).[39] Additionally, the C K-edge spectrum of h-BCN-1 is shown in Figure 2C, which provides clear evidence of C incorporation into the h-BN skeleton. The presence of the peak at 285.4 eV (π* C–C), corresponding to the π* state of graphite, indicates that there was adjacent C in h-BCN-1. The peak located at 286.5 eV and 288.5 eV assigned to C–B bonds and C–N bonds, respectively, were related to the formation of a ternary B–C–N compound.

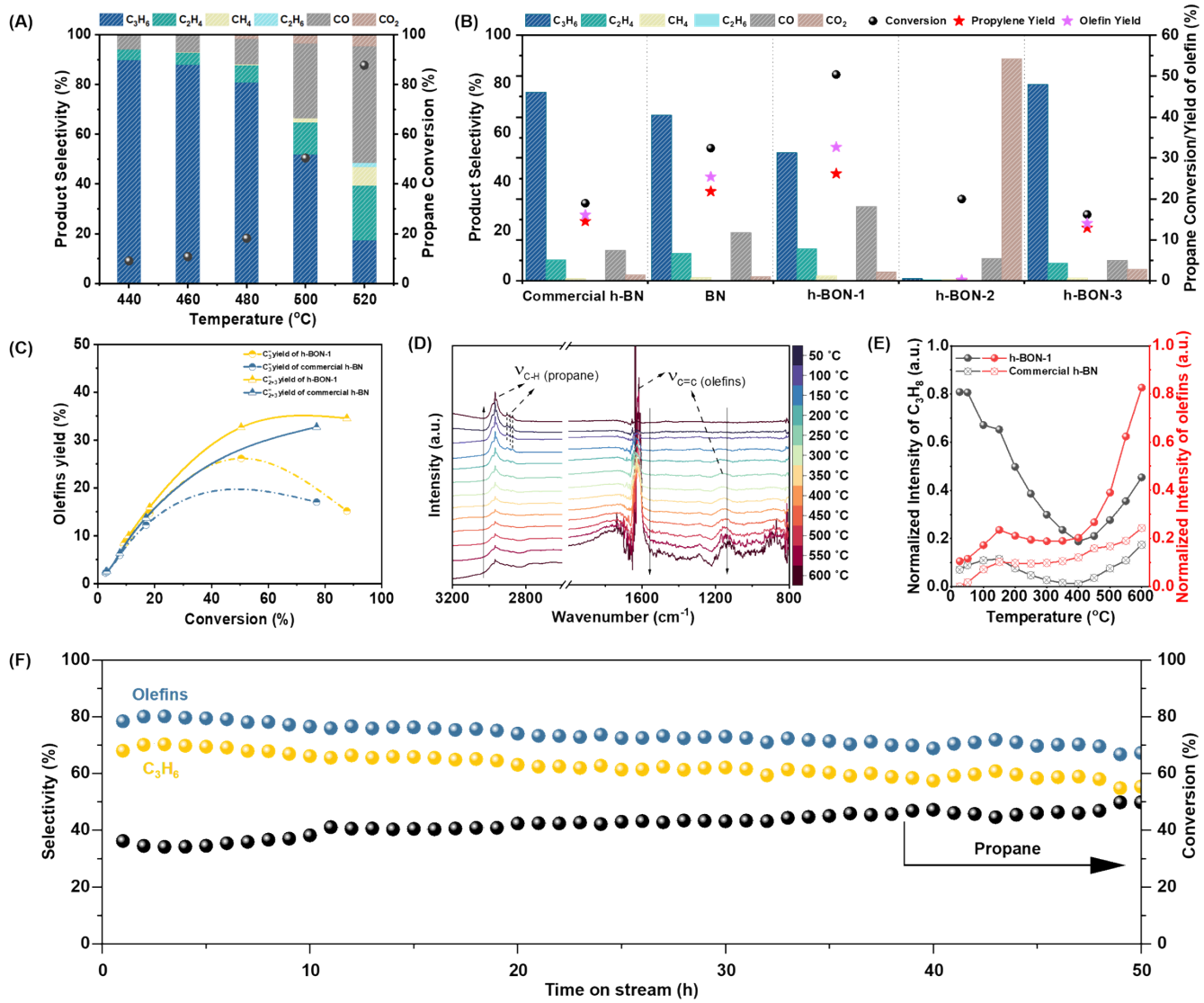

Figure 3. (A) Propane conversion and propylene selectivity with increasing reaction temperature over h-BON-1. (B) Propane conversion, propylene yield, total olefin yield, and product selectivity when different catalysts are deployed at 500 °C (commercial h-BN, h-BN, h-BON-1, h-BON-2, and h-BON-3). (C) Propylene yield and olefin yield as a function of propane conversion. (D) In situ DRIFTS observation of h-BON-1 collected under simulated reaction conditions from 25 °C–600 °C with a ramping rate of 50 °C/min. (E) Normalized intensities of the C-H vibration peak and C=C vibration peak. (F) Stability test of h-BON-1 at 500 °C. Reaction conditions: catalyst weight, 200 mg; gas feed, 24 mL min^{-1}; $C_3H_8/O_2/N_2$ with a molar ratio of 1/1.5/3.5; WHSV = 7200 h^{-1}. Propylene selectivity and olefin selectivity as a function of propane conversion.

The broad peak at approximately 291 eV corresponded to the transitions from C 1s to σ* states (σ* C–C) and the empty higher-energy states, indicating the presence of *p*-symmetry components projected onto the C sites.[40] The O K-edge XANES spectra of h-BON-1 provided additional evidence that the B–O species in h-BON-1 were B–O_3 structures that were structurally distinct from the bulk B_2O_3 on the surface (Figure 2D). The O K-edge XAS spectra of fresh h-BON-1 showed a minor signal at ~532 eV attributed to a B–O bond, which differed from the B–O bond in B_2O_3 (~536 eV), in agreement with a previous report.[18,41] In contrast, except for the B–O peak at 532 eV, there was a peak centered at 535.5 eV, which split into two peaks: $B(OH)_xO_{3-x}$ species (likely BO_3) at 535.2 eV and O–O species at 535.9 eV. The chemical compositions and coordination states were further characterized by XPS, and the results are shown in Figure 2E-2H and Figure S13- S16. The existence of B–N bonds in h-BCN was verified by the peak in the XPS spectra of B 1 s at a binding energy (BE) of 190.5 eV and N1s at a BE of 398.1 eV. Additionally, a peak at a BE of 189.7 eV in the B1s XPS spectrum was attributed to the formation of B–C bonds, and the peak at a BE of 398.8 eV in the N1s XPS spectrum was attributed to the C–N bond (Figure 2E-2F).[38,42] Surface C was incorporated in the form of C–B, C–C, C–N, and C–O bonds, with BEs of 282.7, 284.8, 286.3, and 288.9 eV, respectively, as shown in the C1s XPS spectrum (Figure 2G).[43] XPS results of h-BON-1 revealed the presence of both B–N and N–B in the B 1s and N 1s spectra, respectively, confirming that the h-BN skeleton composed of B and N atoms remained dominant. The doped C atoms in the terminal groups and adjacent locations of h-BCN-1 were substituted by O atoms after oxidation, resulting in oxygen-functionalized h-BON-1, which was confirmed by the appearance of abundant BO_x species. As shown in Figure 2H, the peak at 533.5 eV in the O 1s XPS spectrum was assigned to the $B(OH)_xO_{3-x}$ species, and the peak at 532.1 eV was attributed to B–N/B–O.[24] Notably, another peak at ~532.9 eV belongs to the O–O species, which is likely generated from the O-substitution of adjacent C–C atoms, as corroborated by the FTIR and XPS spectra (Figure 1C, Figure S15-S16).

The ODHP is a vital alternative to traditional propylene production procedures because of its reaction endothermicity and cost-effectiveness. The B-based catalysts played a crucial role in this process, as the B–O active species accounted for propane activation and the unique behavior of O_2 activation on the active surface, leading to high olefin selectivity. To increase the catalytic activity, maximizing the B–O species was essential. We employed h-BON-x catalysts, which utilize a flexible C embedding-O replacement strategy to transfer B–C_3 to B–O_3 active species, for efficient ODHP within a temperature range of 440–520 °C. Notably, h-BON-x catalysts function effectively for ODHP without requiring additional activation. As illustrated in Figure 3A and Figure S17, commercial h-BN, h-BN and h-BON-1 catalysts exhibited poor propane conversion at lower reaction temperatures. This limitation arose from the difficulty in overcoming the energy barrier for the homolytic dissociation of the BO–H bond at low reaction temperatures (<460 °C). Increasing the reaction temperature drastically enhanced propane conversion, yielding remarkable propylene and olefin yields of 26.2% and 32.7%, respectively, and a propane conversion of 50.4% over h-BON-1 at 500 °C under a WHSV of 7,200 h^{-1}, which was much greater than that of commercial h-BN (16.9% propane conversion and 13.7% olefin yield) and h-BN without any C-to-O switch (35.8% propane conversion and 27.1% olefin yield) under the same conditions (Figure 3B-3C). Importantly, the CO_2 selectivity was less than 5% throughout the whole process, and the products were mainly propylene and ethylene. Thus, it was concluded that the flexible and controllable C embedding-O replacement strategy used to transfer B–C_3 to B–O_3 in the h-BN skeleton contributed to the enhanced ODHP performance. When h-BON-2 was tested, minimal propylene with a majority of CO_2 was detected, where a propane conversion of 20.0% and only a low olefin yield of 0.169% were obtained at 500 °C. However, further increasing the C content induced carbonization. h-BON-3 only showed an olefin yield of 14.0%, with a propane conversion of 16.2%. These results confirmed that the incorporation of a suitable number of C atoms was beneficial for constructing h-BON nanostructures that enhanced ODHP activity. Conversely, an excess of C atoms may lead to reduced activity, likely due to surface blockage of the agglomeration of h-BON-2 and h-BON-3 (Figure S17).

To further investigate the mechanism of propane activation and propylene formation, in situ DRIFTS was conducted (Figure 3D). In the absorption stage for introducing C_3H_8, the characteristic vibration peak at approximately 3,060–2,850 cm^{-1} was attributed to the C–H stretching of the methyl and methylene groups in C_3H_8.[44] The intensities of these characteristic peaks were used to assess the C_3H_8 adsorption capacity of h-BON-1, which outperformed that of commercial h-BN (Figure S18). As the treatment temperature increased, the intensity of C–H in C_3H_8 for h-BON-1 decreased more rapidly than that of commercial h-BN. In addition, all the catalysts generated olefins, as indicated by peaks at 1,200–1,000 cm^{-1} and 1,500—1,650 cm^{-1}, corresponding to the stretching vibration of $=CH_2$.[45] The generation rate of $=CH_2$ was relatively fast on the h-BON-1 catalyst, indicating a relatively high consumption rate of C_3H_8 and a relatively high formation rate of olefins (Figure 3E). Additionally, the requirement for high catalytic stability was indispensable. We further applied the optimal h-BON-1 catalyst for ODHP, which showed compelling catalytic activity and stability, as displayed in Figure 3F. After 50 h of operation, propane conversion increased from 34.5% to 50.4%, accompanied by a slight decrease in propylene and olefin selectivity. Moreover, this catalyst demonstrated high activity in ODHP, nearly surpassing other B-based catalysts used in previous studies at the same reaction temperature (500 °C) (Figure S19). The HRTEM images of the spent catalyst suggested that the h-BN nanosheet-like structure remained intact after the reaction, which was consistent with the diffraction peaks in the XRD pattern and FTIR spectra (Figure S4, Figure S20-S22). Additionally, the spectra of the BN_xO_{3-x} species in h-BON-1 before and after ODHP were similar, with a slight increase in intensity at lower δ_{iso} values associated with BO_3 species and the disappearance of BN_3, suggesting further oxidation and the loss of some boron sites after ODHP (Figure S23).

Density functional theory (DFT) calculations were performed to elucidate the active structure and mechanism

of the h-BON catalyst. Based on our characterization analysis, six different types of models were considered, including O–O, BO–ON+B–O, B–O_3, N_2–B–O, N–B_2–O, and B–O edge models (Figure S24). Initially, these models were constructed to identify the one that provides the most stable adsorption configuration for C_3H_8. As displayed in Figure S25, the B–O_3 model was the most stable active site for ODHP, as evidenced by its lowest C_3H_8 adsorption energy for both configurations horizontal and vertical to the surface (E_{ads} of –2.11 eV and -1.98 eV, respectively), which is consistent with the C_3H_8–temperture programmed desorption curves (Figure S26A). Additionally, charge density differences and the relative electron localization function (ELF) contours revealed significant chemisorption between the B atom and C_3H_8 at the B–O_3 site, indicating strong and favorable interactions (Figure 4A). The optimized B–O_3 site was selected for further evaluation of the following C_3H_8 dehydrogenation reaction involving O_2 to produce C_3H_6, while the B–O–edge site was chosen for comparison, as shown in Figure 4B. The ODHP process was initiated with the adsorption of propane, which proceeded as a thermodynamically favorable step for both the B–O_3 and B–O–edge sites, with adsorption energies of -2.117 eV and -0.795 eV, respectively. Following previous studies, the subsequent step in ODHP was considered to start with H abstraction from the secondary carbon (–CH_2–). Based on the relative free energy diagram, the step with the highest uphill energy is defined as the rate-limiting step. Therefore, the rate-limiting step on the B–O_3 site was the first H abstraction of C_3H_8, with a reaction energy of 1.93 eV. To drive the formation of propylene from propyl on the B–O_3 surface, O_2 was introduced in the following step by first abstracting H from the surface O–H/B–H with a reaction energy of 0.90 eV, which simultaneously reduces O_2 to HO_2; this is followed by H_2O_2 formation by HO_2 abstracting the hydrogen from the propyl. Finally, both propylene and H_2O_2 desorbed readily from the surface, and H_2O_2 decomposed to form water (Figure S26B), thereby closing the cycle and regenerating the active site.[46] In contrast, even though a series of thermodynamically downhill steps occurred for the ODHP reaction over the B–O–edge site, the rate-limiting step for the B–O–edge site was C_3H_7*+HO_2*→ C_3H_6*+H_2O_2*, with a high reaction energy of 3.08 eV. Consequently, the B–O_3 site was more thermodynamically favorable than the B–O–edge site for O_2-assisted C_3H_8 dehydrogenation to propylene.

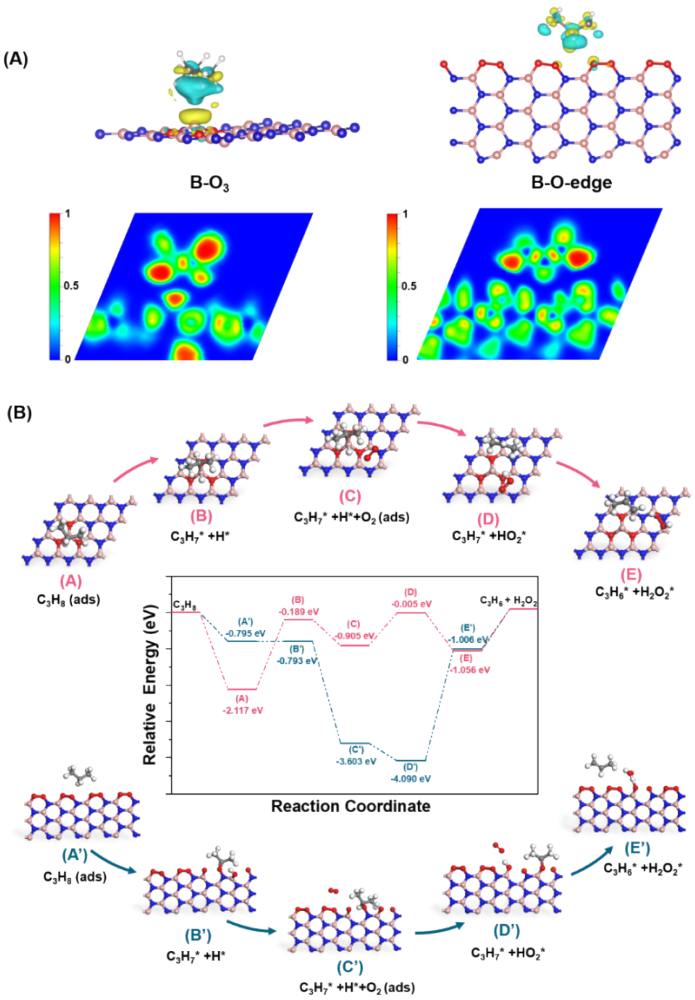

Figure 4. (A) Optimized adsorption model and charge density differences and relative ELF contours of C_3H_8 chemisorbed on the B–O_3 site and B–O–edge site (isosurface level=0.0003). (B) Reaction pathways for the oxidative dehydrogenation of propane to propylene at the B–O_3 site and B–O–edge site and the corresponding atomic configuration (transition states could not be acquired using the current level of theory; thus, quantitative comparisons with experimental data cannot be obtained from our model).

In summary, the successful creation of $B–O_3$ active sites for ODHP in the h-BN skeleton was achieved through a controllable in situ carbon-to-oxygen switch strategy using molten salts ($NaNH_2$, $NaBH_4$ and CaC_2) as precursors. The construction of a high number of $B–O_3$ species in the h-BN structure resulted in an attractive performance in the ODHP process, achieving a propane conversion of 50.4% and an olefin yield of 32.7% at 500 °C, almost surpassing those of previously reported h-BN materials. Furthermore, the original h-BN skeleton was preserved in the BON, providing structural advantages that ensured long-term stability over 50 h at 500 °C during ODHP on stream. This efficient strategy not only facilitates the engineering of active sites in h-BN, which are conducive to the formation of $B–O_3$ active centers to increase ODHP but also provides a novel synthesis capable of providing easy access to BCN nanostructures with a controlled composition and good crystallinity.

ASSOCIATED CONTENT

Supporting Information

The Supporting Information is available free of charge on the ACS Publications website, including experimental procedures, supplementary contents and figures.

AUTHOR INFORMATION

Corresponding Author

*chenhaoch@hnu.edu.cn (H. Chen)
*renbohua@csu.edu.cn (B. Ren)
*dais@ornl.gov (S. Dai)

Author Contributions

All authors have given approval to the final version of the manuscript.

Notes

The authors declare no competing financial interests.

ACKNOWLEDGMENT

H.C. was supported by the National Key R&D Program of China (2023YFB4103000), the Provincial Natural Science Foundation of Hunan (2023JJ40115). S.D. was supported by the U.S. Department of Energy, Office of Science, Office of Basic Energy Sciences, Chemical Sciences, Geosciences, and Biosciences Division, Catalysis Science Program. X. Z was supported by Hunan Provincial Innovation Foundation for Postgraduate (QL20230106). B. R. was supported by National Natural Science Foundation of China (22402230).

REFERENCES

1. Amghizar, I.; Vandewalle, L. A.; Van Geem, K. M.; Marin, G. B., New Trends in Olefin Production. *Engineering* **2017,** *3* (2), 171–178.
2. Lavrenov, A. V.; Saifulina, L. F.; Buluchevskii, E. A.; Bogdanets, E. N., Propylene production technology: Today and tomorrow. *Catal. Ind.* **2015,** *7* (3), 175–187.
3. Carter, J. H.; Bere, T.; Pitchers, J. R.; Hewes, D. G.; Vandegehuchte, B. D.; Kiely, C. J.; Taylor, S. H.; Hutchings, G. J., Direct and oxidative dehydrogenation of propane: from catalyst design to industrial application. *Green. Chem.* **2021,** *23* (24), 9747–9799.
4. Ma, Y.; Song, S.; Liu, C.; Liu, L.; Zhang, L.; Zhao, Y.; Wang, X.; Xu, H.; Guan, Y.; Jiang, J.; Song, W.; Han, Y.; Zhang, J.; Wu, P., Germanium-enriched double-four-membered-ring units inducing zeolite-confined subnanometric Pt clusters for efficient propane dehydrogenation. *Nat. Catal.* **2023**, *6*, 506–518
5. Nakaya, Y.; Hayashida, E.; Asakura, H.; Takakusagi, S.; Yasumura, S.; Shimizu, K.-I.; Furukawa, S., High-Entropy Intermetallics Serve Ultrastable Single-Atom Pt for Propane Dehydrogenation. *J. Am. Chem. Soc.* **2022,** *144* (35), 15944–15953.
6. Ali Hussain Motagamwala, R. A., James Wortman, Valentina Omoze Igenegbai, Suljo Linic, Stable and selective catalysts for propane dehydrogenation operating at thermodynamic limit. *Science* **2021,** *373*, 217–222.
7. Rawan Almallahi, J. W., Suljo Linic, Overcoming limitations in propane dehydrogenation by codesigning catalyst-membrane systems. *Science* **2024,** *383*, 1325–1331.
8. Sattler, J. J. H. B.; Ruiz-Martinez, J.; Santillan-Jimenez, E.; Weckhuysen, B. M., Catalytic Dehydrogenation of Light Alkanes on Metals and Metal Oxides. *Chem. Rev.* **2014,** *114* (20), 10613-10653.
9. Liu, J.; Liu, Y.; Ni, Y. M.; Liu, H. C.; Zhu, W. L.; Liu, Z. M., Enhanced propane dehydrogenation to propylene over zinc-promoted chromium catalysts. *Catal. Sci. Technol.* **2020,** *10* (6), 1739–1746.
10. Liu, Y.; Feng, W.; Li, T.; He, H.; Dai, W.; Huang, W.; Cao, Y.; Fan, K., Structure and catalytic properties of vanadium oxide supported on mesocellulous silica foams (MCF) for the oxidative dehydrogenation of propane to propylene. *J. Catal.* **2006,** *239* (1), 125–136.
11. Vajda, S.; Pellin, M. J.; Greeley, J. P.; Marshall, C. L.; Curtiss, L. A.; Ballentine, G. A.; Elam, J. W.; Catillon-Mucherie, S.; Redfern, P. C.; Mehmood, F.; Zapol, P., Subnanometre platinum clusters as highly active and selective catalysts for the oxidative dehydrogenation of propane. *Nat. Mater.* **2009,** *8* (3), 213–216.
12. Roy, S.; Zhang, X.; Puthirath, A. B.; Meiyazhagan, A.; Bhattacharyya, S.; Rahman, M. M.; Babu, G.; Susarla, S.; Saju, S. K.; Tran, M. K.; Sassi, L. M.; Saadi, M. A. S. R.; Lai, J.; Sahin, O.; Sajadi, S. M.; Dharmarajan, B.; Salpekar, D.; Chakingal, N.; Baburaj, A.; Shuai, X.; Adumbumkulath, A.; Miller, K. A.; Gayle, J. M.; Ajnsztajn, A.; Prasankumar, T.; Harikrishnan, V. V. J.; Ojha, V.; Kannan, H.; Khater, A. Z.; Zhu, Z.; Iyengar, S. A.; Autreto, P. A. D. S.; Oliveira, E. F.; Gao, G.; Birdwell, A. G.; Neupane, M. R.; Ivanov, T. G.; Taha-Tijerina, J.; Yadav, R. M.; Arepalli, S.; Vajtai, R.; Ajayan, P. M., Structure, Properties and Applications of Two-Dimensional Hexagonal Boron Nitride. *Adv. Mater.* **2021,** *33* (44), 2101589.
13. Roudi, M. R. R.; Ranjkesh, M.; Korayem, A. H.; Shahsavary, R., Review of Boron Nitride Nanosheet-Based Composites for Construction Applications. *ACS Appl. Nano Mater.* **2022,** *5* (12), 17356–17372.
14. Chen, H.; Jiang, D. E.; Yang, Z.; Dai, S., Engineering Nanostructured Interfaces of Hexagonal Boron Nitride-Based Materials for Enhanced Catalysis. *Acc. Chem. Res.* **2023,** *56* (1), 52–65.
15. Sainsbury, T.; Satti, A.; May, P.; Wang, Z.; McGovern, I.; Gun'Ko, Y. K.; Coleman, J., Oxygen Radical Functionalization of Boron Nitride Nanosheets. *J. Am. Chem. Soc.* **2012,** *134* (45), 18758–18771.
16. Li, Y.; Jiang, P.; Lyu, X.; Li, X.; Qi, H.; Tang, J.; Xue, Z.; Yang, H.; Lu, G.; Sun, Q.; Hu, X.; Gao, Y.; Gong, Q., Revealing low-loss dielectric near-field modes of hexagonal boron nitride by photoemission electron microscopy. *Nat. Commun.* **2023,** *14* (1), 4837.
17. Grant, J. T.; Carrero, C. A.; Goeltl, F.; Venegas, J.; Mueller, P.; Burt, S. P.; Specht, S. E.; McDermott, W. P.; Chieregato, A.; Hermans, I., Selective oxidative dehydrogenation of propane to propene using boron nitride catalysts. *Science* **2016,** *354*, 1570–1573.
18. Love, A. M.; Thomas, B.; Specht, S. E.; Hanrahan, M. P.; Venegas, J. M.; Burt, S. P.; Grant, J. T.; Cendejas, M. C.; McDermott, W. P.; Rossini, A. J.; Hermans, I., Probing the Transformation of Boron Nitride Catalysts under Oxidative Dehydrogenation Conditions. *J. Am. Chem. Soc.* **2019,** *141* (1), 182–190.
19. Shi, L.; Wang, D.; Song, W.; Shao, D.; Zhang, W.-P.; Lu, A.-H., Edge-hydroxylated Boron Nitride for Oxidative Dehydrogenation of Propane to Propylene. *ChemCatChem* **2017,** *9* (10), 1788–1793.
20. Tian, J.; Collinge, G.; Yuk, S. F.; Lin, J.; Glezakou, V.-A.; Lee, M.-S.; Wang, Y.; Rousseau, R., Dynamically Formed Active Sites on Liquid Boron Oxide for Selective Oxidative Dehydrogenation of Propane. *ACS Catal.* **2023**, 8219–8236.
21. Zhang, X.; Huang, Y.; Zhou, W.; Luo, Q.; Huang, Y.; Luo, X.; Dai, J.; Chen, H.; Fu, J., Controllable Growing Defects in Cambered Boron Nitride Utilizing a Plane Bending Strategy for Efficient Oxidative Dehydrogenation of Propane. *ACS Catal.* **2024**, 15418–15428.
22. Tian., J.; Tan., J.; Xu., M.; Zhang., Z.; Wan., S.; Wang., S.; Lin., J.; Wang., Y., Propane oxidative dehydrogenation over highly selective hexagonal

boron nitride catalysts: The role of oxidative coupling of methyl. *Sci. Adv.* **2019,** *5*, eaav8063.
23. Venegas, J. M.; McDermott, W. P.; Hermans, I., Serendipity in Catalysis Research: Boron-Based Materials for Alkane Oxidative Dehydrogenation. *Acc. Chem. Res.* **2018,** *51* (10), 2556–2564.
24. Li, P.; Zhang, X.; Wang, J.; Xue, Y.; Yao, Y.; Chai, S.; Zhou, B.; Wang, X.; Zheng, N.; Yao, J., Engineering O–O Species in Boron Nitrous Nanotubes Increases Olefins for Propane Oxidative Dehydrogenation. *J. Am. Chem. Soc.* **2022,** *144* (13), 5930–5936.
25. Lu, W. D.; Wang, D. Q.; Zhao, Z. C.; Song, W.; Li, W. C.; Lu, A. H., Supported Boron Oxide Catalysts for Selective and Low-Temperature Oxidative Dehydrogenation of Propane. *ACS Catal.* **2019,** *9* (9), 8263–8270.
26. Mark, L. O.; Dorn, R. W.; McDermott, W. P.; Agbi, T. O.; Altvater, N. R.; Jansen, J.; Lebrón-Rodríguez, E. A.; Cendejas, M. C.; Rossini, A. J.; Hermans, I., Highly Selective Carbon-Supported Boron for Oxidative Dehydrogenation of Propane. *ChemCatChem* **2021,** *13* (16), 3611–3618.
27. Chen, H.; Yang, Z.; Guo, W.; Dunlap, J. R.; Liang, J.; Sun, Y.; Jie, K.; Wang, S.; Fu, J.; Dai, S., From Highly Purified Boron Nitride to Boron Nitride-Based Heterostructures: An Inorganic Precursor-Based Strategy. *Adv. Funct. Mater.* **2019,** *29* (50), 1906284.
28. Lei, W.; Portehault, D.; Dimova, R.; Antonietti, M., Boron Carbon Nitride Nanostructures from Salt Melts: Tunable Water-Soluble Phosphors. *J. Am. Chem. Soc.* **2011,** *133* (18), 7121–7127.
29. Huang, C.; Chen, C.; Zhang, M.; Lin, L.; Ye, X.; Lin, S.; Antonietti, M.; Wang, X., Carbon-doped BN nanosheets for metal-free photoredox catalysis. *Nat. Commun.* **2015,** *6* (1), 7698.
30. Zhang, X.; Duan, Z.; Wu, Y.; Qiu, T.; Shi, X., Sintering-resistant and highly active boron oxide doped B_xCuZrO_2 catalyst for catalytic diethanolamine dehydrogenation. *Chem. Eng. Sci.* **2021,** *246*, 116897.
31. Shayan Angizi, M. A. A., Maryam Darestani-Farahani, and Peter Kruse, Review–Two-Dimensional Boron Carbon Nitride: A Comprehensive Review. *ECS J. Solid State Sci. Technol.* **2020,** *9*. 083004.
32. Wang, S.; Zhang, L.; Xia, Z.; Roy, A.; Chang, D. W.; Baek, J. B.; Dai, L., BCN Graphene as Efficient Metal-Free Electrocatalyst for the Oxygen Reduction Reaction. *Angew. Chem. Int. Ed.* **2012,** *51* (17), 4209–4212.
33. Li, D.; Bi, J.; Xie, Z.; Kong, L.; Liu, B.; Fan, X.; Xiao, X.; Miao, Y.; Zhao, Z., Flour-derived borocarbonitride enriched with boron–oxygen species for the oxidative dehydrogenation of propane to olefins. *Sci. China Chem.* **2023,** *66* (8), 2389–2399.
34. Xiao, F.; Naficy, S.; Casillas, G.; Khan, M. H.; Katkus, T.; Jiang, L.; Liu, H.; Li, H.; Huang, Z., Edge-Hydroxylated Boron Nitride Nanosheets as an Effective Additive to Improve the Thermal Response of Hydrogels. *Adv. Mater.* **2015,** *27* (44), 7196–7203.
35. Cendejas, M. C.; Paredes Mellone, O. A.; Kurumbail, U.; Zhang, Z.; Jansen, J. H.; Ibrahim, F.; Dong, S.; Vinson, J.; Alexandrova, A. N.; Sokaras, D.; Bare, S. R.; Hermans, I., Tracking Active Phase Behavior on Boron Nitride during the Oxidative Dehydrogenation of Propane Using Operando X-ray Raman Spectroscopy. *J. Am. Chem. Soc.* **2023,** *145* (47), 25686–25694.
36. Portehault, D.; Giordano, C.; Gervais, C.; Senkovska, I.; Kaskel, S.; Sanchez, C.; Antonietti, M., High-Surface-Area Nanoporous Boron Carbon Nitrides for Hydrogen Storage. *Adv. Funct. Mater.* **2010,** *20* (11), 1827–1833.
37. Chen, S.; Li, P.; Xu, S.; Pan, X.; Fu, Q.; Bao, X., Carbon doping of hexagonal boron nitride porous materials toward CO_2 capture. *J. Mater. Chem. A.* **2018,** *6* (4), 1832–1839.
38. Kim, S. Y.; Park, J.; Choi, H. C.; Ahn, J. P.; Hou, J. Q.; Kang, H. S., X-ray Photoelectron Spectroscopy and First Principles Calculation of BCN Nanotubes. *J. Am. Chem. Soc.* **2007,** *129* (6), 1705–1716.
39. McDougall, N. L.; Partridge, J. G.; Nicholls, R. J.; Russo, S. P.; McCulloch, D. G., Influence of point defects on the near edge structure of hexagonal boron nitride. *Phys. Rev. B.* **2017,** *96* (14), 144106.
40. Ray, S. C.; Tsai, H. M.; Chiou, J. W.; Jan, J. C.; Kumar, K.; Pong, W. F.; Chien, F. Z.; Tsai, M. H.; Chattopadhyay, S.; Chen, L. C.; Chien, S. C.; Lee, M. T.; Lin, S. T.; Chen, K. H., X-Ray absorption studies of boron–carbon–nitrogen ($B_xC_yN_z$) ternary alloys. *Diam. Relat. Mater.* **2004,** *13* (4-8), 1553–1557.
41. Caretti, I.; Jiménez, I., Influence of carbon content and nitrogen vacancies on the bonding structure and mechanical performance of graphite-like BC_xN thin films. *J. Appl. Phys.* **2012,** *112* (6), 063525.
42. Chen, H.; Yang, S. Z.; Yang, Z.; Lin, W.; Xu, H.; Wan, Q.; Suo, X.; Wang, T.; Jiang, D. E.; Fu, J.; Dai, S., Sinter-Resistant Nanoparticle Catalysts Achieved by 2D Boron Nitride-Based Strong Metal-Support Interactions: A New Twist on an Old Story. *ACS Cent. Sci.* **2020,** *6* (9), 1617–1627.
43. Ahsan, M. A.; He, T.; Eid, K.; Abdullah, A. M.; Curry, M. L.; Du, A.; Puente Santiago, A. R.; Echegoyen, L.; Noveron, J. C., Tuning the Intermolecular Electron Transfer of Low-Dimensional and Metal-Free BCN/C_{60} Electrocatalysts via Interfacial Defects for Efficient Hydrogen and Oxygen Electrochemistry. *J. Am. Chem. Soc.* **2021,** *143* (2), 1203–1215.
44. Cheng, X.; Zhang, Y.; Wang, J.; Zhang, X.; Sun, C.; Yang, Y.; Wang, X., B–O Oligomers or Ring Species in AlB_2: Which is More Selective for Propane Oxidative Dehydrogenation? *ACS Catal.* **2023,** *13* (3), 1630–1637.
45. Wang, C.; Fang, W.; Liu, Z.; Wang, L.; Liao, Z.; Yang, Y.; Li, H.; Liu, L.; Zhou, H.; Qin, X.; Xu, S.; Chu, X.; Wang, Y.; Zheng, A.; Xiao, F. S., Fischer–Tropsch synthesis to olefins boosted by MFI zeolite nanosheets. *Nat. Nanotechnol.* **2022,** *17* (7), 714–720.
46. Zhang, X.; You, R.; Wei, Z.; Jiang, X.; Yang, J.; Pan, Y.; Wu, P.; Jia, Q.; Bao, Z.; Bai, L.; Jin, M.; Sumpter, B.; Fung, V.; Huang, W.; Wu, Z., Radical Chemistry and Reaction Mechanisms of Propane Oxidative Dehydrogenation over Hexagonal Boron Nitride Catalysts. *Angew. Chem. Int. Ed.* **2020,** *59* (21), 8042–8046.

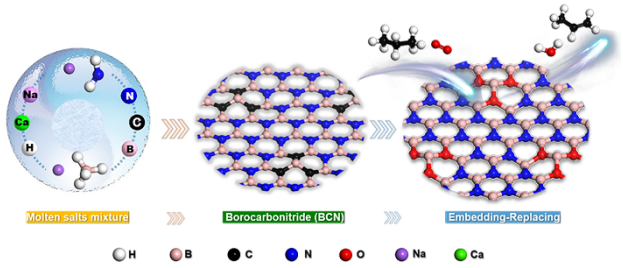
Na
N
Ca
C
H
B
Molten salts mixture
Borocarbonitride (BCN)
Embedding-Replacing
H
B
C
N
O
Na
Ca